Breakdown of Near-Surface Sea Current from High-Frequency Radar Data

Alejandro Cáceres-Euse, Anne Molcard, Natacha Bourg, Dylan Dumas, Charles-Antoine Guérin, Giovanni Besio

Breakdown of Near-Surface Sea Current from High-Frequency Radar Data

ALEJANDRO CÁCERES-EUSE,[a,b] ANNE MOLCARD,[a] NATACHA BOURG,[a] DYLAN DUMAS,[a] CHARLES-ANTOINE GUÉRIN,[a] AND GIOVANNI BESIO[b]

[a] *MIO, Université de Toulon, Aix-Marseille University, CNRS, IRD, Toulon, France*
[b] *Department of Civil, Chemical and Environmental Engineering, University of Genoa, Genoa, Italy*

(Manuscript received 9 February 2022, in final form 27 July 2022)

ABSTRACT: To assess the contribution of wind drag and Stokes drift on the near-surface circulation, a methodology to isolate the geostrophic surface current from high-frequency radar data is developed. The methodology performs a joint analysis utilizing wind field and in situ surface currents along with an unsupervised neuronal network. The isolation method seems robust in the light of comparisons with satellite altimeter data, presenting a similar time variability and providing more spatial detail of the currents in the coastal region. Results show that the wind-induced current is around 2.1% the wind speed and deflected from the wind direction in the range [18°, 23°], whereas classical literature suggests higher values. The wave-induced currents can represent more than 13% of the ageostrophic current component as function of the wind speed, suggesting that the Stokes drift needs to be analyzed as an independent term when studying surface sea currents in the coastal zones. The methodology and results presented here could be extended worldwide, as complementary information to improve satellite-derived surface currents in the coastal regions by including the local physical processes recorded by high-frequency radar systems. The assessment of the wave and wind-induced currents have important applications on Lagrangian transport studies.

KEYWORDS: Atmosphere-ocean interaction; Ocean circulation; Surface observations

1. Introduction

The surface ocean currents result from complex physical processes forced by ocean–atmosphere energetic fluxes (such as momentum and heat fluxes), and traditionally, solved by the superposition of several current components. These components include the wind-induced current, the wave-induced Stokes drift, the geostrophic current, tidal currents, among others (Pedlosky 1987; Kundu et al. 2012; Kumar et al. 2017; Berta et al. 2018). Ocean currents are assumed mostly in geostrophic balance when considering large-scale processes (larger than tens of kilometers) (Hernández-Carrasco and Orfila 2018), while ageostrophic currents play a more relevant role at smaller spatial scales (such as coastal areas) (Donlon 2013). It has been observed that geostrophic currents have important implications on marine debris accumulation, whereas wind-induced currents and Stokes drift influence oil spill transport, search and rescue, and passive tracer trajectories (Ardhuin et al. 2009; Onink et al. 2019; van der Mheen et al. 2020). Nonetheless, the contribution by wind-induced currents and Stokes drift on the surface ocean current at local/regional scale is still poorly known.

In the literature, several methodologies are utilized in estimating geostrophic velocities. For instance, optimization functions applied to velocity profiles (ADCPs) in order to separate the current components (Roach et al. 2015), or information from altimeter satellite missions combined with in situ data (ADCP moorings, gliders, and drifters-derived velocities) (Poulain et al. 2012; Rio et al. 2014; Carret et al. 2019). Nonetheless, still, there are several limitations when trying to use altimeter products (from available satellite missions) such as a strong land interference on the signal inside the coastal area within the first 50 km offshore (Albuquerque et al. 2018), and the spatial resolution from altimeter maps is too coarse to capture fine flow features.

Regarding the wind-induced current and Stokes drift, previous studies have utilized drifters-derived information (Kirwan et al. 1979; Poulain et al. 2012; Chang et al. 2012; Rio et al. 2014), high-frequency radars (HFR) (Mao and Heron 2008; Ardhuin et al. 2009; Chavanne 2018; van der Mheen et al. 2020) and a combination between in situ and synthetic information (from numerical models) (Tamtare et al. 2022) to estimate the wind and wave effects on the surface current. However, most of these studies performed wind and Stokes drift estimation assuming the rest of the current components (i.e., geostrophic currents, inertial oscillations, and tides) negligible or weak, assumptions that can be wrong in enclosed basins such as the Mediterranean Sea, where mesoscale surface currents are dominated by geostrophic balance (Poulain et al. 2012; Hernández-Carrasco and Orfila 2018). For instance, Ardhuin et al. (2009) used HFR data along with wave modeling to show that the total surface current can be considered as the superposition of the Stokes drift and an Eulerian current. The Eulerian component was assumed to be influenced by inertial and tidal currents and weakly influenced by the geostrophic current component. On the other hand, Rio et al. (2014) used drifters-derived information and satellite data to present a methodology to estimate the near-surface (and subsurface) ocean current at global scale. The latter methodology is based on the superposition of the geostrophic balance and an empirical Ekman model, and the authors remarked that regional-/local-scale processes are not considered in the calculation due to the nature of the data used. In situ information, such as HFR data can be considered in order to include these local-scale

Corresponding author: Alejandro Cáceres-Euse, alejandro.caceres-euse@univ-tln.fr

DOI: 10.1175/JTECH-D-22-0013.1

effects. In addition, the Stokes drift contribution was not included in the analysis.

From this background, it is clear that the role of the Stokes drift and wind-induced current on the surface sea current at local/regional scale (coastal regions) should be better captured, and the previous estimations can be influenced by strong assumptions. To partially address these issues, we develop a methodology to isolate the main current components from the HFR data, and to determine a relationship between local wind, wave field, and the surface current.

To take a step forward in this understanding, the aim of this work is to answer two main questions: 1) Is it possible to develop a methodology to estimate the geostrophic surface current component by using in situ HFR data? And 2) by subtracting the geostrophy from the measured surface current, can this methodology help to determine the contribution by waves and wind drag on the surface sea current? To answer these fundamental questions, we apply the self-organizing map (SOM) technique to HFR surface current data along with wind data from an atmospheric model. SOM is an unsupervised neural network, extensively applied to the oceanography field in order to recognize circulation features such as gyres and upwelling/downwelling processes at sea (Liu and Weisberg 2005b, 2007; Liu et al. 2007; Orfila et al. 2021), or as a tool to fill missing data in HFR systems (Hernández-Carrasco et al. 2018). SOM is capable of capturing nonlinear processes in the data (Liu and Weisberg 2005b). In addition, it has been presented as a powerful tool to develop ocean current forecast systems (Vilibić et al. 2016), showing promising results when comparing against physics-based ocean models. Then, one could think of a way to analyze the HFR currents with the wind fields in order to extract targeted surface sea current features (Mihanović et al. 2011). The analysis can allow a breakdown of the total current into the geostrophic component and the near-surface wind-driven component. Later, the assessment of the contribution by the wave-induced current can be determined by focusing on the ageostrophic surface current component. The HFR (measured currents) includes the geostrophic component as well as tidal-, wind-, and wave-driven components (Lorente et al. 2022; Reyes et al. 2022), making these observations perfectly suitable for our breakdown analysis.

This paper is structured as follows: The study site and the HFR setup are presented in section 2. The data preprocessing is described in section 3. The methodology of the surface current decomposition and the use of SOM on the HFR data to isolate the main current components is presented in section 4. Section 5 presents the estimation and validation of the geostrophic current. The assessment of the ageostrophic component is described in section 6. Finally, section 7 shows the discussion and conclusions.

2. Study site and HFR system

The Toulon Bay area (delimited by the region shown in Fig. 1) is located on the southern coasts of France, in the northwestern Mediterranean Sea. It is a urbanized zone, with several socioeconomic activities such as fishery and tourism, and the largest military port in France. Also, this highly anthropized

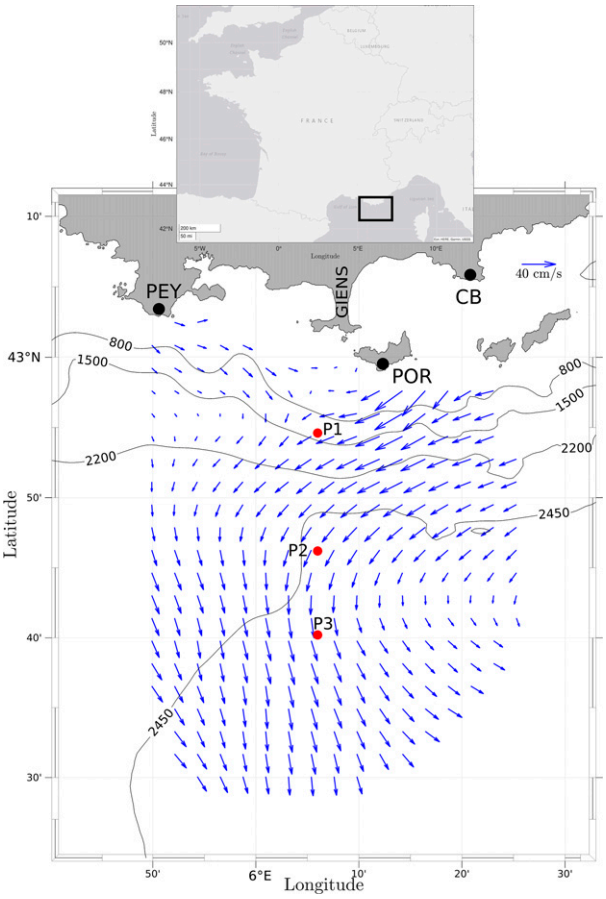

FIG. 1. View of the Toulon Bay area (black rectangle) and location of the three HFR stations (black circles). The blue arrows show a snapshot of the measured surface current for 10 Jun 2020. The contours are the isobaths for 800, 1500, 2200, and 2450 m depth. P1, P2, and P3 are used to compare time series.

area includes a preserved area of the National Park of Port-Cros (Rey et al. 2020). The geographic configuration of the region presents a steep continental shelf, going from tens of meter in the bay to several hundreds of meters offshore, and is composed by a semienclosed bay, the Giens Peninsula (GIENS), and several capes and islands. The region is characterized by the dominant well-known boundary Northern Current (NC) that determines the main kinematic conditions (Shrira and Forget 2015), the semidiurnal and diurnal tidal motions (12 and 24 h, respectively) and an inertial frequency band centered around 17.6 h. The NC is part of the general cyclonic circulation of the western Mediterranean basin (Millot 1999), showing a clear spatial and temporal variability due to complex coastline shapes, atmospheric forcing and (sub)mesoscale structures (Ourmières et al. 2011; Guihou et al. 2013; Bourg and Molcard 2021). So the NC can reach speeds up to 1 m s^{-1}, and can be close to the shore or away from it depending on the season (Millot 1989; Petrenko 2003; Ourmières et al. 2018). Concerning the atmospheric conditions, the dominant winds blow from west

and east. Westerly/northwesterly (called mistral) winds are cold and dry, and easterly winds are warm and humid. These two wind regimes can be strong (>10 m s^{-1}) and persistent during the year, while calm weather conditions occur when the wind speed is lower than 5 m s^{-1} (Mazoyer et al. 2020). In general, from winter to fall the waves come from east–northeast (ENE) and west–northwest (WNW) reaching heights up to 6 m (see Fig. A1 in the appendix). During summer the waves come predominately from WNW presenting the smallest wave height values, whereas the highest values are present during winter coming from ENE.

This study site is equipped with a WERA HFR system manufactured by Helzel GmbH. The system is composed of two transmitters (TX) and two receivers (RX) located on three distant sites in the Toulon Bay area (see Fig. 1). A first TX–RX station is located in Fort Peyras (PEY). It works in a quasi-monostatic configuration with a 2-antenna transmitting end-fire array and a linear 12-antenna receiving array. The second station is a standalone transmitter composed of a single monopole antenna located at the south of Porquerolles Island (POR). The third station is composed of a 12-antenna receiving array in Cap Bénat (CB). This network operates in multistatic configuration (Guérin et al. 2019; Dumas et al. 2020) and provides four elliptical projections of the surface currents corresponding to the four possible TX–RX combinations. The radar operates at a central frequency $f = 16.15$ MHz with an available sweep band of 100 kHz allowing for a 1.5 km range resolution. Surface current mapping is obtained by applying improved direction finding techniques (Dumas and Guérin 2020) to the receiving arrays, leading to high-resolution radial maps of about 1° azimuthal resolution. The total surface velocity and its Cartesian components are obtained every hour by recombination of the best two radials (POR/CB and PEY/PEY) and projected onto a regular Cartesian grid of 1 km resolution using a weighted interpolation technique. In addition, quality checks and consistency tests have been performed in the voltage-to-current conversion while processing the radar data, as well as a processing suite including the bistatic current extraction for each radial map, the signal-to-noise ratio threshold definition, and the geometric dilution of precision (GDOP) (Dumas et al. 2020). Then, several drifter's campaigns have been used to validate the measurements (Guérin et al. 2019).

3. Data preprocessing

a. HFR surface velocity field

Comparisons in June 2019 (Dumas et al. 2020) and November 2020 (not published yet) have shown a good agreement between the radar-derived surface currents and the in situ CARTHE drifters (Novelli et al. 2017), whose integration depth of about 60 cm is similar to the HFR one (Stewart and Joy 1974), under the assumption of a linear velocity profile. Particularly, when averaging over all drifters launches (five and eight in 2019 and 2020, respectively), it is observed a root-mean-square difference on the order of 5–7 cm s^{-1} for the hourly zonal component and 8–9 cm s^{-1} for the meridional one. The differences are induced by an increment in the absolute magnitude of currents during the fall and winter periods, and a large excursion of the drifters toward the borders of the HFR coverage. The signal-to-noise ratio of the radar signal is minimal at the borders of the HFR domain (by definition), reducing the accuracy of the retrieved surface currents in these limiting regions. In the present study, we use 6 months of hourly HFR observations surveyed in 2020, from 1 June to 30 November. This period was selected because the velocity maps cover more than 75% of the time every month. First, the Data Interpolating Empirical Orthogonal Functions (DINEOF) gap-filling algorithm (Alvera-Azcárate et al. 2005) was applied to the radial velocity maps to complete missing data in the HFR domain and to replace noisy velocity values. This algorithm calculates the main modes of the data variability by means of the empirical orthogonal functions (EOFs), and then, those are used to fill gaps by an iterative method. Before determining the EOFs, data from the nonmissing regions were removed to apply a cross validation. Then, by means of comparisons between the dataset and the reconstructed data the number of EOFs was set to 197, retaining 97% of the variance and obtaining a correlation between the original and reconstructed velocities above 0.95. Later, the data were low-pass filtered using 3 days cutoff to remove high-frequency signals (such as inertial oscillations, Stokes drift, tides, among others) (Rio et al. 2014) and resampled to 3 h to match the wind time resolution. The DINEOF computation, convergence, and application to the HFR dataset can be found in Bourg and Molcard (2021).

b. Wind data and wind-induced current

The wind field at 10 m height ($\mathbf{U}_{10}$) comes from the Application of Research to Operations at Mesoscale (AROME) wind model. AROME is a nonhydrostatic 3D high-resolution numerical model, operational at Météo-France since December 2008. The size of the mesh is 1.3 km over France and the outputs available every 3 h. It was designed to improve short range forecasts of severe events such as intense Mediterranean precipitations (Cévenole events), severe storms, fog, urban heat during heat waves. The model has a data assimilation system to include regional observations and outputs from previous forecast models, adapted to the AROME spatial resolution (Brousseau et al. 2016). Additionally, data from the Application Radar à la Météorologie Infrasynoptique (ARAMIS) radar network (Doppler wind and precipitation) are used for model assimilation at local scale on an hourly basis (for details, see http://www.umr-cnrm.fr/). Given its good performance and high temporal and spatial resolution, AROME has been utilized to develop oceanographic forecast models by means of ocean–atmosphere–wave coupled simulations (Sauvage et al. 2021).

To estimate the wind-induced current at the surface ($z = 0$) two methods are used: 1) the classical Ekman theory (u_w^{Ek}), where the surface current is deflected 45° to the right of the wind direction in the Northern Hemisphere (to the left in the Southern Hemisphere) (Kundu et al. 2012); and 2) a modified Ekman formulation (u_w^{Ep}) developed by using drifter trajectories (Rio et al. 2014) (a parametric Ekman model), where the surface current is deflected between 20° and 40° from the wind direction depending on seasonal variability and latitude. Both approaches are based on the fact that the surface current

results from a momentum balance between the wind drag and Coriolis forces (Kirwan et al. 1979; Pedlosky 1987), and the main difference lies on the value of the resultant current direction. Thus, the classical Ekman model is defined as

$$\mathbf{u}_w^{\mathrm{Ek}} = \frac{\boldsymbol{\tau}}{\sqrt{\rho_w^2 A_z f}} e^{i(\alpha-\pi/4)}, \quad f = 2\omega\sin(\phi), \tag{1}$$

where $\boldsymbol{\tau} = \rho_a C_D U_{10}\mathbf{U}_{10}$ is wind shear stress, ρ_a the air density, the drag coefficient $C_D = (0.75 + 0.06U_{10}) \times 10^{-3}$ (Garrat 1997), α the wind direction, ρ_w the water density, f is the Coriolis parameter, ω the angular velocity of Earth (equal to 7.292×10^{-5} (rad s^{-1}), ϕ the latitude, and A_z the vertical eddy viscosity in the water. In this study A_z is assumed constant (Polton et al. 2005; Mao and Heron 2008) and equal to 0.1071 m^2 s^{-1} (Morales-Márquez et al. 2021; Roach et al. 2015).

The parametric Ekman model from Rio et al. (2014) is based on the amplitude and phase factors (β and θ, respectively),

$$\mathbf{u}_w^{\mathrm{Ep}} = \beta(z)\boldsymbol{\tau}e^{i\theta(z)}, \tag{2}$$

where θ represents the deviation of the surface current from the wind direction. These two parameters were defined based on the fitting analysis to undrogued drifters for comparison with the HFR currents, so that $\beta \approx 0.73$ m^2 s kg^{-1} and $\theta \approx 18°$.

c. *Wave-induced current*

The wave-induced current component, the Stokes drift ($\mathbf{u}_s$), depends on the wave energy spectrum distribution and local water depth; however, analytical solutions have proven that the estimation of $\mathbf{u}_s$ based on bulk wave parameters can give good estimations, specifically, in the near-surface region (Kenyon 1969; Kumar et al. 2017). So, in this study, the WAVEWATCH III (WWIII) model (Tolamn 2009) was employed to generate hindcasts at the Toulon Bay, and the Stokes drift computations are performed by using bulk wave parameters resultant from the wave model. Thus, $\mathbf{u}_s = u_s\mathbf{k}$ is estimated as

$$\mathbf{u}_s = \frac{H_s^2}{16}\mathbf{k}\sigma e^{-2kz}, \quad \mathbf{k} = k[\cos(\theta_w), \sin(\theta_w)], \tag{3}$$

where θ_w is the mean wave direction of propagation, σ is the wave radian frequency, H_s is the significant wave height and $\mathbf{k}$ the wavenumber vector, and z the depth measured from the surface downward. Additionally, at the near-surface, e^{-2kz} is close to 1 and

$$u_s \approx \frac{H_s^2}{16}k\sigma. \tag{4}$$

Before the estimation of $\mathbf{u}_s$, the WWIII was calibrated and validated using in situ information (buoys) and satellite data. A complete description of the model performance, numerical settings and the methodology applied during the model calibration and validation is presented in Lira-Loarca et al. (2022). The wave simulation was carried out by using a triangle-unstructured computational grid covering the entire Mediterranean Sea with varying spatial resolution (see Fig. 2). The overall spatial resolution of the mesh is about 25 km offshore increasing toward the coast of Toulon up to 300 m. Finally, the outputs of the wave parameters were obtained every 3 h.

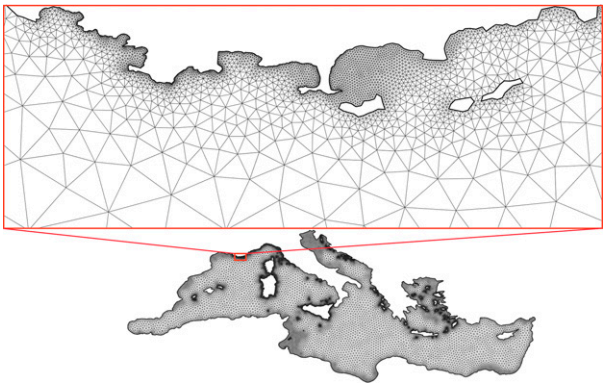

FIG. 2. Triangular-unstructured grid for the wave modeling and the zoom-in at the Toulon Bay.

4. Methods

a. *Components of the total surface sea current*

At local/regional scales, the speed and direction of the currents near the surface can be, mainly, determined by a linear superposition (Tamtare et al. 2022) of the geostrophic current ($\mathbf{u}_g$), wind-induced current ($\mathbf{u}_w$), Stokes drifts ($\mathbf{u}_s$), and any outer current transported by the mean flow into the local area ($\mathbf{u}_\epsilon$),

$$\mathbf{u}_t = \mathbf{u}_g + \mathbf{u}_w + \mathbf{u}_s + \mathbf{u}_\epsilon, \tag{5}$$

where $\mathbf{u}_t$ is the total current measured by the HFR.

For the calculation of $\mathbf{u}_g$, the surface flow is assumed stationary and the frictional forces due to wind drag are negligible (including wave generation), so that the momentum equilibrium is balanced by the Coriolis force and the pressure gradient (Pedlosky 1987). In the study site, $\mathbf{u}_g$ obeys the large-scale circulation processes at the Mediterranean Sea scale, described by the NC's dynamic (Poulain et al. 2012; Guihou et al. 2013; Carret et al. 2019). Now, the sum of $\mathbf{u}_s + \mathbf{u}_w$ is defined as the local ageostrophic component ($\mathbf{u}_a$) of the near-surface sea current, since they rise from the ocean–atmosphere interaction, and $\mathbf{u}_\epsilon$ represents the surface current not easily related to wind-/wave-induced currents [such as residual circulation or (sub)mesoscale processes generated locally or transported by the mean flow].

To estimate each component, a decomposition method that consists of three phases is performed: assessment of the geostrophic component $\mathbf{u}_g$, assessment of the wind-induced current component, and estimation of $\mathbf{u}_s$ to complete the ageostrophic component $\mathbf{u}_a$. This decomposition starts by training the SOM to determine a neuron under negligible atmospheric forcing conditions and then finding the snapshots of the velocity field represented by the aforementioned neuron where a dominant geostrophic balance may be considered. Later, $\mathbf{u}_a$ is determined by applying Eq. (5).

b. Self-organizing map analysis

The SOM is an unsupervised learning neural network especially suited to extract patterns in large datasets. SOM is a nonlinear pattern and classification tool used to map high-dimensional input data onto a two-dimensional space, while preserving the topological relationships between the input data (Liu et al. 2006). The input data are clustered in units, called neural units. The number of units is the same as the size of the SOM array (or lattice), where each unit has a weight vector (m_i) that has the number of components equal to the dimension of the input sample data.

The learning process algorithm consists of the presentation of the input data to the SOM during an iterative process. In each iteration the unit whose weight vector is the closest (the smallest Euclidian distance) to the presented input data is selected as the winner unit [best matching unit (BMU)],

$$c_k = \min\|X_k - m_i\|, \tag{6}$$

where $\|\cdot\|$ is the distance measure, c_k is an index of the BMU on the SOM related to the snapshot data k, and c is the location of the BMU in the lattice map (previously defined). During the training iteration, the BMU is moved (updated) along with its topological neighborhoods toward the input sample, where the topological neighboring units are modified based on a neighborhood function h. In this study, the batch version of the SOM algorithm (in Vesanto et al. 2000) has been used. This setting allows us to use simultaneously all the input data to update the weight vectors, and provides lower quantization (QE) and topographic errors (TE) while keeping a computational efficiency (Liu and Weisberg 2005b; Liu et al. 2006; Mihanović et al. 2011),

$$m_i(t+1) = \frac{\sum_{j=1}^{M} n_j h_{ij}(t)\overline{X}_j}{\sum_{j=1}^{M} n_j h_{ij}(t)}, \tag{7}$$

where M is the size of the lattice, $\overline{X}_j$ is the mean of the n data vectors in group j, and $h_{ij}(t)$ represents the neighborhood function value at unit j centered on the unit i. For h, the Epanechnikov neighborhood function has been defined, since it presents better result for the batch training function based on average QE and TE (Liu and Weisberg 2005b; Mihanović et al. 2011).

5. Geostrophic current estimation

a. Assessment of u_g using SOM analysis

To determine the neuron under negligible atmospheric forcing conditions, the input data used are the total surface currents measured by the HFR system ($\mathbf{u}_t$) and the wind $\mathbf{U}_{10}$. The $\mathbf{u}_t$ and $\mathbf{U}_{10}$ were daily averaged to perform a joint SOM spatial analysis. The parameters for SOM were defined as follows: a hexagonal lattice structure (Hernández-Carrasco et al. 2018) and linear initialization (based on the first two leading EOFs) (Liu and Weisberg 2007), along with a radius of 1 for the neighborhood function and a 3 × 2 lattice array. The radius and lattice array were found after several training runs, trying to obtain the lowest QE and TE, while gathering the negligible atmospheric forcing conditions in only one neuron. The lower QE and TE, the better the SOM training (a better BMU fitting) (Liu et al. 2006).

The resultant SOM array is arranged such that the most dissimilar patterns are located the farthest away from each other (e.g., neurons 1 and 6), while the more similar the closer. Now, the 6 patterns identified by SOM (see Fig. 3) represent characteristic features of the near-surface current and its associated wind conditions. The timeline can be described as N5 → N3 → N6 → N1 → N4 → N2. N2 and N5 are transitional stages (during 31.7% of the time) associated with mid-magnitude westerly winds that reduce the NC speed and modify its direction, generating a reversal flow at the lower part of N2 and upper part of N5. N3 and N6 (28.4% of the time) show an NC tilted southward following the wind direction when strong westerly winds are blowing (mistral events). N1 represents an intense NC due to the influence of a strong easterly wind (during 11.5% of the time). Westerly winds occur more often than easterly ones [as observed in the climatology study by Rey et al. (2020)]. These five conditions have been previously reported and analyzed by several studies in the region, such as Guihou et al. (2013), Berta et al. (2018), Carret et al. (2019), and Molcard et al. (2021). Finally, N4 occurs during dates in which the wind changes its direction (from westward to eastward) or during calm wind conditions, showing a near-surface current not affected by wind drag forces (negligible wind conditions) and a boundary current only altered by land constraints. The wind speed is lower than 2 m s^{-1} and the surface current goes from east to west centered around 42.8° latitude. Thus, N4 is the targeted neuron representing a dominant geostrophic balance condition.

b. Influence of u_a on the estimation of u_g

After selecting the targeted neuron for the assessment of u_g, it is necessary to determine the influence of u_a on N4. To do so, a comparison between u_t (HFR surface current) and u_a on three radar points (P1, P2, and P3) along the latitudinal axis of the HFR was done (see Fig. 1—red circles for stations deployment). P1 was selected close to the coast, P2 located inside the most stable position of the NC and P3 is outside the NC vein. u_a was determined using the snapshots (dates) of the wind field represented by N4 (the BMU time series—see Fig. A2 in the appendix) for u_w^{Ek} [Eq. (1)]; and u_s [Eq. (3)] was low-pass filtered (using a 3 day cutoff) and daily averaged, so that the swell at the surface current was evaluated for the same dates. Figure 4 shows this comparison. In addition, a second comparison using the neurons under nonnegligible atmospheric conditions, following the same procedure, is also shown.

The resultant comparison (in Fig. 4) shows the magnitude of u_t and u_a for N4 in the left panel, and the rest of the neurons in the right panel. During N4 conditions, neither the wind-induced current nor the Stokes drift play a relevant role on the surface current. In fact, u_a is close to zero for the three

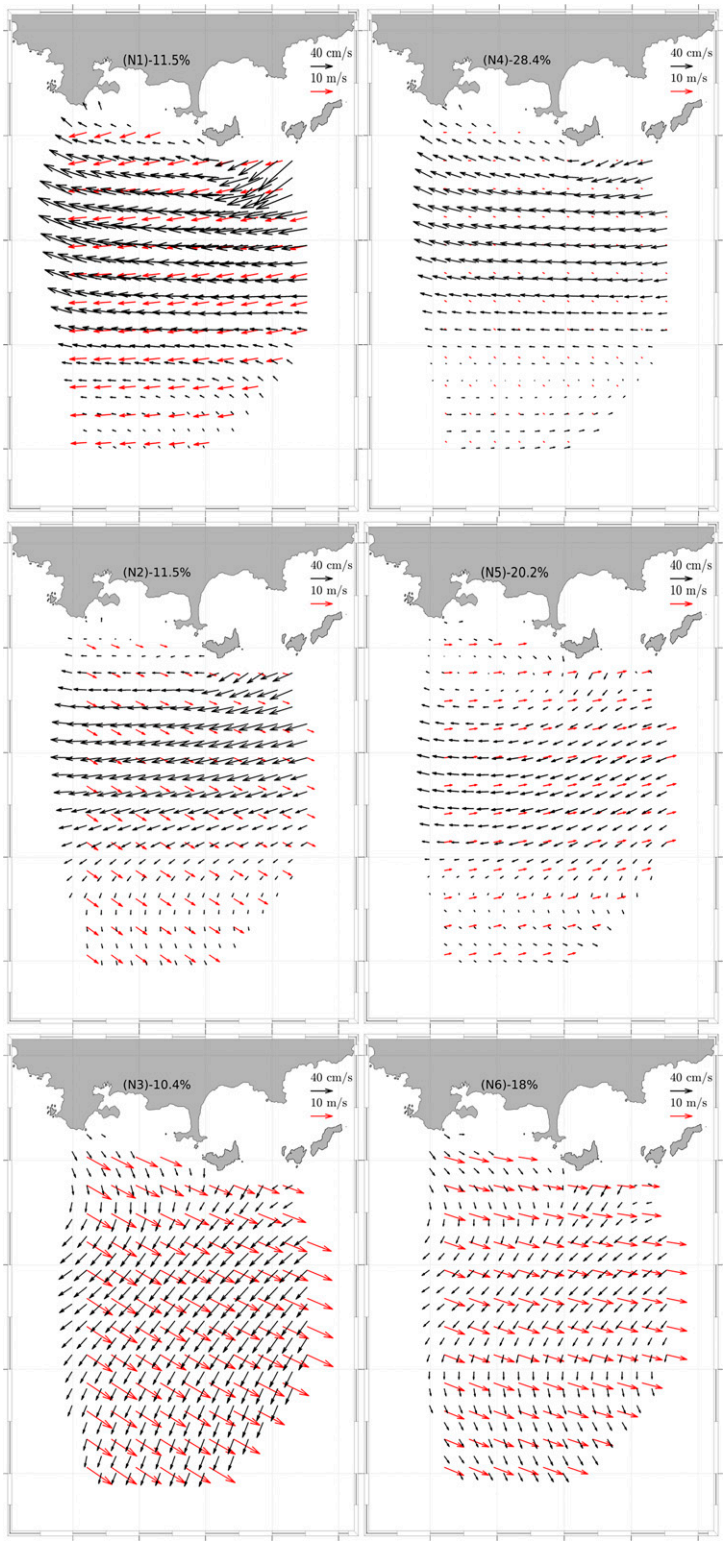

FIG. 3. The 3 × 2 joint SOM analysis for u_t and U_{10} from June to November 2020. Black arrows are the HFR surface current and red arrows the wind field at 10 m height. N4 represents a negligible atmospheric forcing conditions (<2 m s^{-1}), while the rest of the neurons show patterns under nonnegligible wind condition (>5 m s^{-1}).

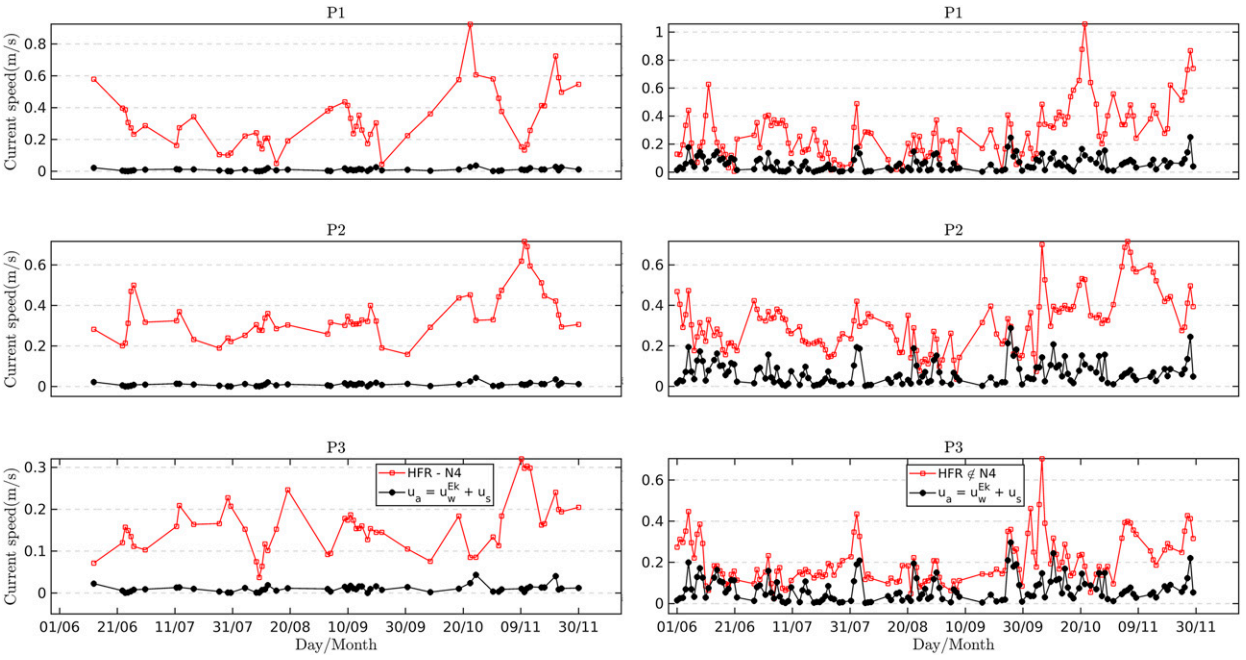

FIG. 4. Influence of u_a on (left) negligible (N4) and (right) nonnegligible atmospheric conditions (N1, N2, N3, N5, N6). Red color is u_t and black color is u_a. During this phase u_t and u_s were low-pass filtered using a 3 day cutoff. u_a, u_s, and u_t refer to the magnitude of the velocity fields.

stations, having values lower than 10% of u_t. The u_a reaches a maximum value of 4.5 cm s^{-1} on P3 between the period 22–28 October, less than 50% of u_t. Thus, given that under negligible atmospheric forcing conditions u_a is very weak compared to u_t, one can consider the near-surface current dominated by geostrophic balance; therefore, the geostrophic component can be defined as $u_g \approx u_t$ for N4.

Regarding the rest of the neurons (Fig. 4—right panel), the comparison shows u_t and u_a with the same order of magnitude, u_a reaches values as high as 60% of u_t (or more), for instance, from 31 July to 30 September on P3, or from early June to mid-July for P1 and P3. These neurons have an important contribution by the atmospheric forcing and, at the same time, by u_g. An estimated residual $u_t - u_a$ gives values close to u_g in N4 (not shown), related to an increment in the right panel when u_a is high. Then, to assess the ageostrophic component in Eq. (5), u_g needs be to subtracted from u_t (for these neurons).

c. *Validation of estimated u_g against satellite-derived data*

The satellite product SEALEVEL_EUR_PHY_L4_NRT_OBSERVATIONS_008_060 provides daily absolute geostrophic velocities (UVG) on a 0.125° × 0.125° spatial grid worldwide. UVG is calculated using information from the sea level anomalies (SLA) and absolute dynamic topography (ADT) measured by all the available altimeter missions (i.e., *Jason-3*, *Sentinel-3A*, *HY-2A*, *SARAL*/AltiKa, *CryoSat-2*, *Jason-2*, *Jason-1*, T/P, *Envisat*, *GFO*, and *ERS-1*/*-2*). Then, once the influence of u_a (composed by wind drag and swell waves) was verified to be insignificant under negligible atmospheric forcing conditions and u_g was determined from N4, a comparison against satellite-derived information was performed in order to validate the estimated u_g.

The comparison was done as follows: 1) by using time series from the closest satellite data to P1, P2, and P3; and 2) a spatial comparison using monthly averaged velocity fields, applying a conditional averaging to u_g. For the temporal comparison, P1, P2, and P3 were conveniently selected to be close to satellite nodes. For the conditional averaging by month, only the velocity snapshots with BMU equal N4 were utilized, excluding the velocity maps with a significant u_a contribution. See Fig. 5 for the time series and Fig. 6 for the monthly averaging comparisons.

The comparison in Fig. 5 shows u_g and the satellite records with a similar time variability. A stronger current speed is present from October to November (during fall) than that observed from June to September (summer). In summer the currents on P1 and P2 are centered around 0.2 m s^{-1} and P3 around 0.1 m s^{-1}, while in fall P1 and P2 are around 0.4 m s^{-1} and P3 around 0.2 m s^{-1}. This trend implies that the geostrophic current doubles its magnitude from summer to fall [in agreement with glider records in Carret et al. (2019) for 2010–16]. In addition, station P2 presents the best agreement with the satellites, followed by P3 and by P1. The estimated u_g on P2 and P3 is capable of reproducing the oscillations in the geostrophic current (e.g., 11 July–9 November for P2 and 13 June–10 August for P3), whereas on P1 the variance of u_g is higher for the HFR than that in the satellite data (mid-June or fall). P2 and P3 present some overestimations during summer and fall, but smaller than those observed on P1. Finally, given that P1 is the closest station to the coastal margins available on the satellite grid (20 km to POR), the

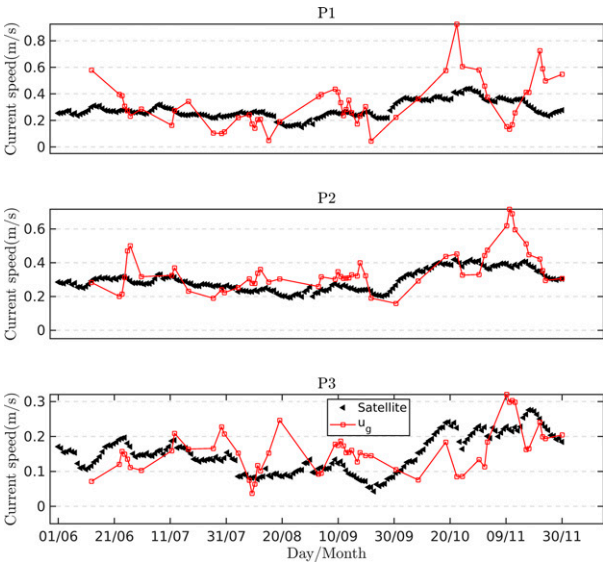

FIG. 5. Comparison of time series for u_g (N4) vs satellite-derived geostrophic current speed for the three stations along the latitudinal axis of the HFR domain. Red color for HFR and black color for satellite.

differences can be associated with effects of land constraints on the surface current, captured by the HFR system but not included in the satellite records (as shown in Fig. 6), in addition to larger errors in the measured velocity field due to low signal-to-noise ratio values at the borders of the HFR coverage.

From the conditional averaging per month, the comparison in Fig. 6, it is possible to observe that not only the geostrophic current speed is well reproduced by the estimated u_g but also its direction. Particularly, the countercurrent traveling eastward in the southern region of the HFR domain and the westward current (the NC) in the central area are well captured. This implies a great progress compared to the standard way of evaluating the u_g from current data, where the whole dataset is used in the averaging procedure [see Fig. A3 in the appendix and Berta et al. (2018)]. The main differences are present when approaching to the coast, where u_g is tilted northwestward and the satellite data are mostly zonal or slightly tilted southwestward (e.g., June, July, September, or October). This deviation in u_g is produced by the presence of islands and the coastline orientation. Now, given the high spatial resolution of the HFR, additional information about the geostrophic current patterns can be provided by u_g. For instance, the cyclonic eddy during August shown by the blue cross in the southern part of the HFR domain, a smaller anticyclonic eddy in November (in the upper part) or the strong shear in the lower part of the velocity map in September. This information cannot be seen with the satellite data, showing the analysis developed in this study as a valuable and complementary tool to understand coastal processes. The conditional monthly averaged u_g is used in the next section for the assessment of u_a.

6. Assessment of the ageostrophic current component

a. Analysis of the wind-induced current

The HFR measures the near-surface sea layer, starting below the air–sea interface and until the end of the turbulent layer, so that the measured wind-induced current component may not be fully balanced by the Coriolis force (Fernandez et al. 1996). This direct wind-induced current can be expressed by a u_w versus U_{10} relationship along with a deflected angle (ψ) smaller than 45°. In fact, in situ studies using HFR and drifters data, observed direct wind-induced currents to be $u_w^d \approx 1\%$ to $4\% \times U_{10}$ (Ardhuin et al. 2009; van der Mheen et al. 2020; Berta et al. 2018; Chang et al. 2012) and ψ in the range [10°–45°] (Rio et al. 2014; Mao and Heron 2008). To verify this assumption we determined u_w^d as follows: first, the conditional monthly averaged $\mathbf{u}_g$ is subtracted from $\mathbf{u}_t$; later, a 3×3 joint SOM training is performed using the resultant velocity maps and $\mathbf{U}_{10}$ as input data. Finally, the velocity snapshots represented by neurons with a clear response to $\mathbf{U}_{10}$ are selected to estimate u_w^d and ψ. For ψ a dot product between $\mathbf{u}_w^d \cdot \mathbf{U}_{10}$ [see Eq. (8)] is applied. The lattice array was defined to extract the features that can be easily associated with the terms in Eq. (5), keeping the minimum number of neurons. Thus, the $u_w^d = f(U_{10})$ expression is compared against u_w^{Ek} and u_w^{Ep}:

$$\psi = \cos^{-1}\left(\frac{\mathbf{u}_w^d \cdot \mathbf{U}_{10}}{u_w^d U_{10}}\right). \tag{8}$$

The 3×3 array depicted in Fig. 7 shows the neurons grouped in three main features. The first group represents the residual surface currents associated with geostrophic balance; so that after removing $\mathbf{u}_g$ from the HFR data, the resultant neurons are characterized by insignificant currents (<2 cm s^{-1}) along with negligible atmospheric forcing conditions (neurons N5, N7, and N9). The second group illustrates the patterns that cannot be, completely, related to local wind-driven currents ($\mathbf{u}_\epsilon$), such as the clockwise vortex observed in N1 or the curved path on the surface current in response to strong mistral in N3. The latter may be associated with Ekman-geostrophic wind response. Finally, the third group represents the wind-driven near-surface currents, either by westerly (N2, N4, and N6) or easterly (N8) wind conditions. The velocity snapshots composing the third group were used to calculate τ. The shear stress is averaged by bins following an incremental step of $\Delta\tau = 0.1$ Pa, and the confidence interval determined using one standard deviation (γ) (following Chang et al. 2012). Then, a linear regression for u_w^d was obtained from the mean τ values (see Fig. 8),

$$u_w^d = 0.34\tau + 0.12, \quad r^2 = 0.98 \quad (5 \le U_{10} \le 14 \text{ m s}^{-1}), \tag{9}$$

with a high correlation coefficient (0.98), and the mean observed ψ, with respect to the wind direction, was found in the range [18°, 23°]. Here, changes in the turbulence mixing can play a relevant role on γ, due to the seasonal variability of the stratification and atmospheric forcing (Dritschel et al. 2020;

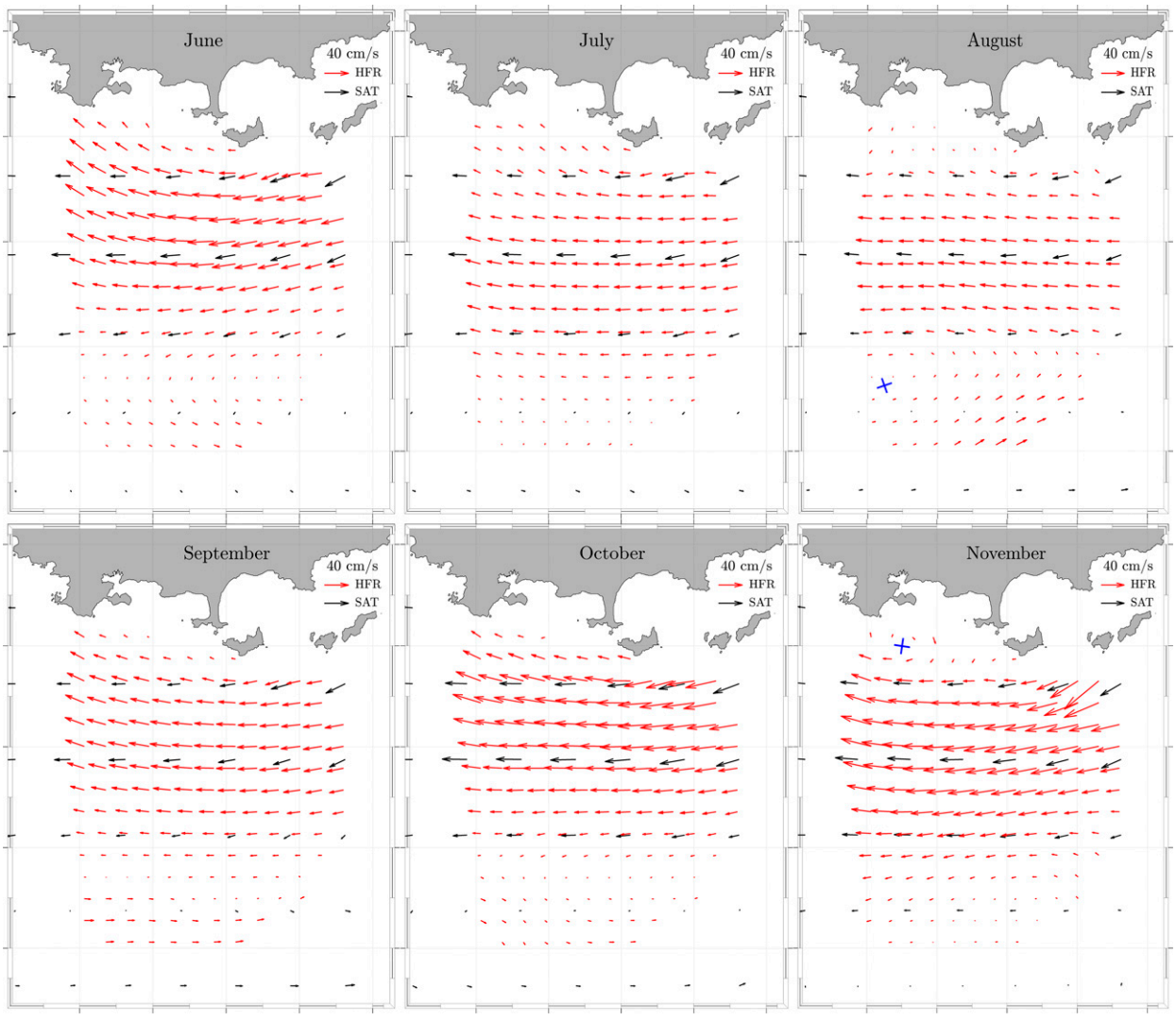

FIG. 6. Comparison of monthly averaged velocity maps from June to November 2020: Estimated $\mathbf{u}_g$ (HFR) vs satellite-derived velocity (SAT). Red color for HFR and black color for satellite data.

Rascle and Ardhuin 2009). ψ presents similar results to those observed by Rio et al. (2014) using undrogued drifters, which could better describe the wind-induced near-surface current, since the surrounding surface sea current is the main driver of undrogued drifters. In addition, the direct wind-induced current can be approximated by $u_w^d \sim 2.1\% \times U_{10}$, a similar factor to that reported in the Toulon Bay area in Berta et al. (2018) by means of a multiplatform observing system.

Now, the comparison against u_w^{Ek} and u_w^{Ep} is performed since Eqs. (1) and (2) are regularly applied to understand and predict the large-scale distribution of floating microplastic in the ocean (Kubota 1994; Martinez et al. 2009; Onink et al. 2019), or to estimate the total surface and subsurface current worldwide (Rio et al. 2014). Here, this comparison is done in order to assess the performance of Eq. (9) against two well-established formulations. Figure 8 (bottom panel) shows u_w^{Ek} always smaller than u_w^d and u_w^{Ep}. This behavior has been observed in Shrira and Almelah (2020) when comparing the classical theory against calculation for a depth varying vertical mixing coefficient model, forced by a time-dependent wind field. Additionally, the stronger the shear (or U_{10}) the lesser the differences between u_w^d and u_w^{Ep}, whereas the difference between u_w^d and u_w^{Ek} keeps constant ($\sim$10 cm s^{-1}). In average, for U_{10} around 6 m s^{-1} u_w^d is twice u_w^{Ep}, while for U_{10} higher than 6 m s^{-1} the difference is lower than 5 cm s^{-1}. So u_w^d seems to present good estimations, particularly when comparing to u_w^{Ep}. Nonetheless, it is important to highlight that even when recent improvements to the Ekman model have been presented, still, this is an open research topic (from the theoretical and practical viewpoint). This problem involves not only the near-surface ocean circulation but also its behavior along the water column as a function of time and space (Shrira and Almelah 2020; Dritschel et al. 2020).

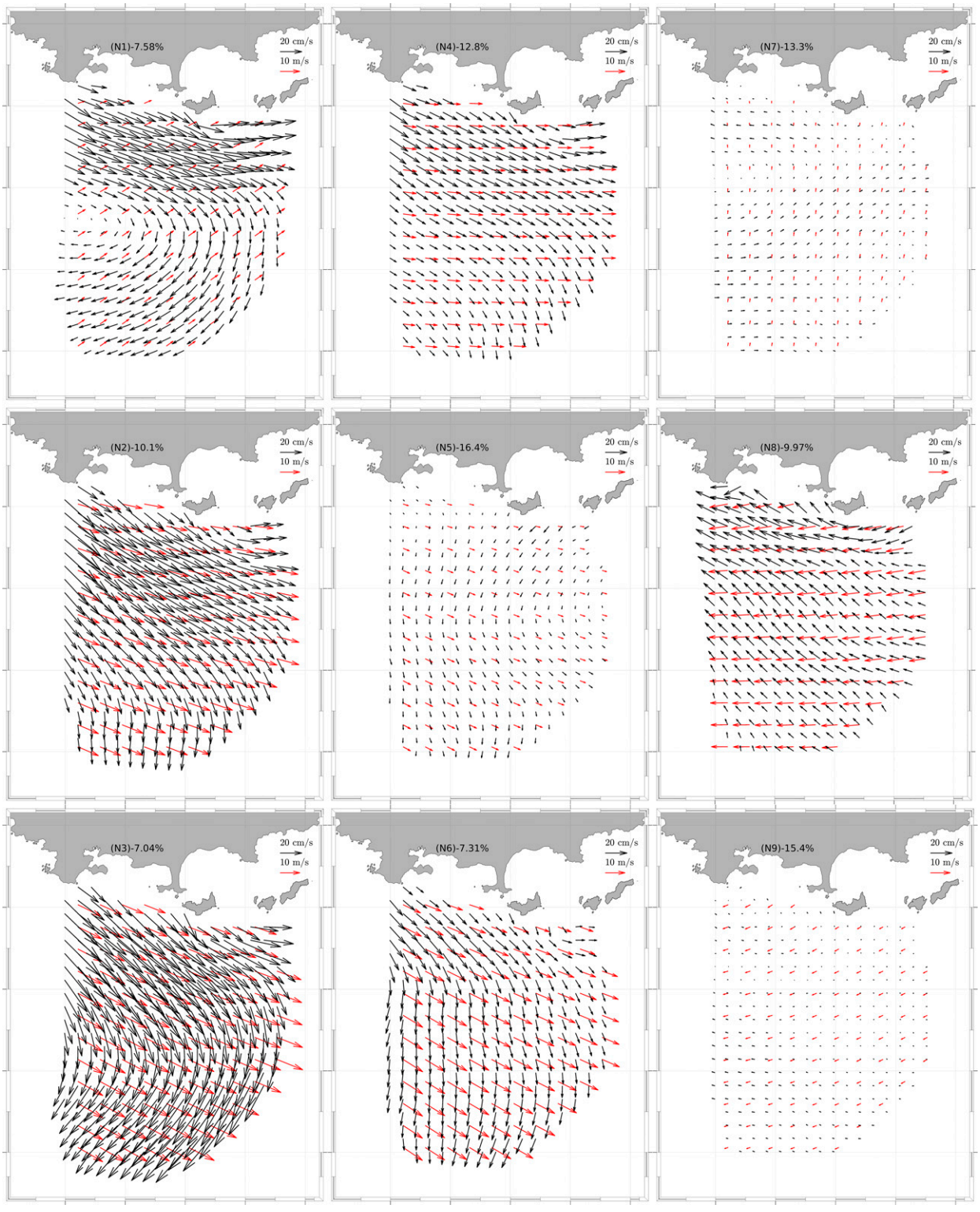

FIG. 7. The 3 × 3 SOM analysis using the $\mathbf{u}_t$–$\mathbf{u}_g$ resultant maps and $\mathbf{U}_{10}$ as input data. The SOM parameters were chosen following the same procedure in section 5. Black color represents the surface current and red color represents the wind field.

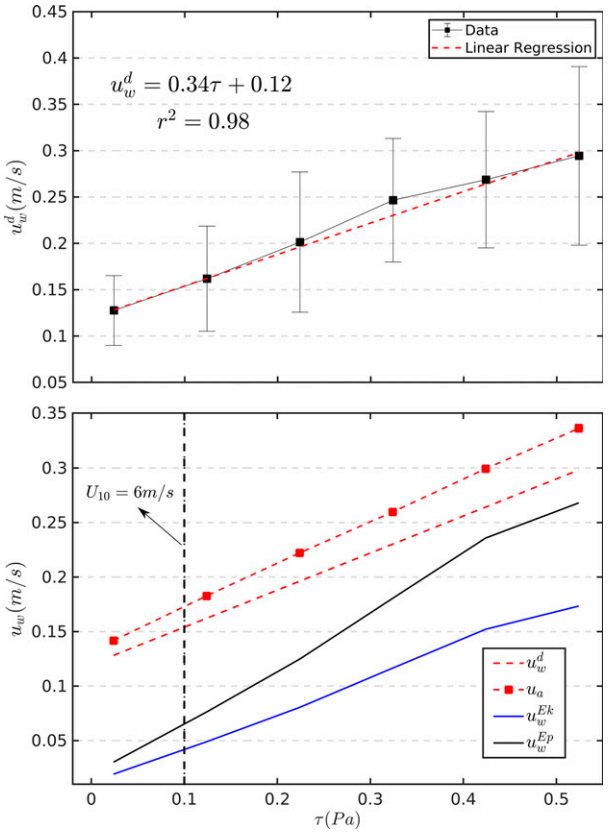

FIG. 8. (top) Direct wind-induced current (u_w^d) as a function of the wind stress τ. The black error bars show plus and minus one standard deviation (γ) and the dashed red line represents the linear regression with a correlation coefficient equal 0.98 ($u_w^d \sim 2.1\% \times U_{10}$). (bottom) A comparison between u_w^d and the two classical wind-induced current formulations (u_w^{Ek} and u_w^{Ep}). u_a is retrieved by adding u_s to u_w^d according to the BMUs for N2, N4, N6, and N8 in the 3×3 lattice.

b. *Stokes drift contribution*

To estimate the contribution of waves to the ageostrophic component, u_s [Eq. (3)] is estimated from the wave maps according to the BMUs (as for the wind-induced current) and then added to u_w^d in Eq. (9) (see Fig. 8, bottom panel). The increment from u_w^d (in %) is referred to here as the contribution by the Stokes drift. At this point, the wave parameters are not low-pass filtered, as previously done in section 5, so that u_a is computed using the original WWIII outputs.

Figure 8 shows a clear effect by u_s on u_a. During weak to mid wind conditions (<6 m s^{-1}), u_s can represent up to 10% of u_a, whereas for mid to strong wind conditions (>6 m s^{-1}) the wave contribution can be above 13%. This result is in agreement with Ardhuin et al. (2009), who found that most of the Stokes drift contribution comes from the high-frequency part of the wave energy spectrum, so that u_s is function of the wind speed U_{10} and H_s. This quantitative comparison shows that the wave effects need to be included as an independent term in the momentum balance equation when predicting the surface currents (as shown in Tamtare et al. 2022), playing a relevant role on the net particle movement at the near-surface ocean (Clarke and Van Gorder 2018).

7. Discussion and conclusions

The aim of this study is to assess the influence of wind drag and Stokes drift on the near-surface circulation based on in situ HFR data, and to introduce a methodology to estimate the geostrophic current component based on an unsupervised neuronal network (SOM). This methodology can be used as complementary information to include regional coastal currents (where satellites can present strong land interference) into global circulation databases. In fact, the $\mathbf{u}_g$ estimation presented here is in agreement with previous studies based on multiplatform systems such as the Copernicus Marine Service Information and Berta et al. (2018), and long-term circulation analysis (Carret et al. 2019; Bourg and Molcard 2021). In addition, the estimation of the geostrophic current from HFR data presents a good advantage compared to satellite data, where the spatial resolution of satellite derived currents does not allow us to observe local circulation patterns at regional scales.

The relationship between the wind and the wind-induced currents found in this study is in agreement with other investigations around the world, such as van der Mheen et al. (2020) for the western Australian region, or Chang et al. (2012) and Shay et al. (2007) for the Pacific and Atlantic coasts. In addition, this relationship gives similar results to those observed using the empirical Ekman model proposed by Rio et al. (2014), including the deflected angle in the range [18°, 23°]. This analysis has important application on offshore industries, search and rescue, oil spill monitoring, among others, given that classical literature suggests $u_w^d \sim 3\% \times U_{10}$ (Bye 1967), while it seems to be closer to $u_w^d \sim 2.1\% \times U_{10}$, affecting drastically the prediction of floating objects.

Equation (9) and Fig. 8 are developed under the assumption of zero lag for the surface current response to wind. This was confirmed by calculations of wind-current cross correlation for several time shifts (from −300 to 300 h), showing the highest correlation coefficient centered at zero time shift (see Fig. A4 in the appendix). This result is in agreement with a similar diagram presented in Mao and Heron (2008). Thus, at 3 h time resolution the assumption is valid; however, this could change if the time resolution of wind and HFR data is increased.

The limitation of this study lies on the fact that the breaking down analysis is performed by finding neurons under negligible atmospheric forcing conditions, so that information about u_w^d for very weak wind scenarios is not well known and the intercept value in Eq. (9) (0.12) could be overestimated. This intercept could be associated with thermal winds response to wind forcing. Thus, it is necessary to include information of the water column in this methodology, to capture the effect of the stratification and vertical gradients on $\mathbf{u}_g$. In addition, the velocity field here analyzed is measured in a deep water region (water depth > 800 m), so that the geostrophic current is mainly driven by horizontal density gradients and, in less

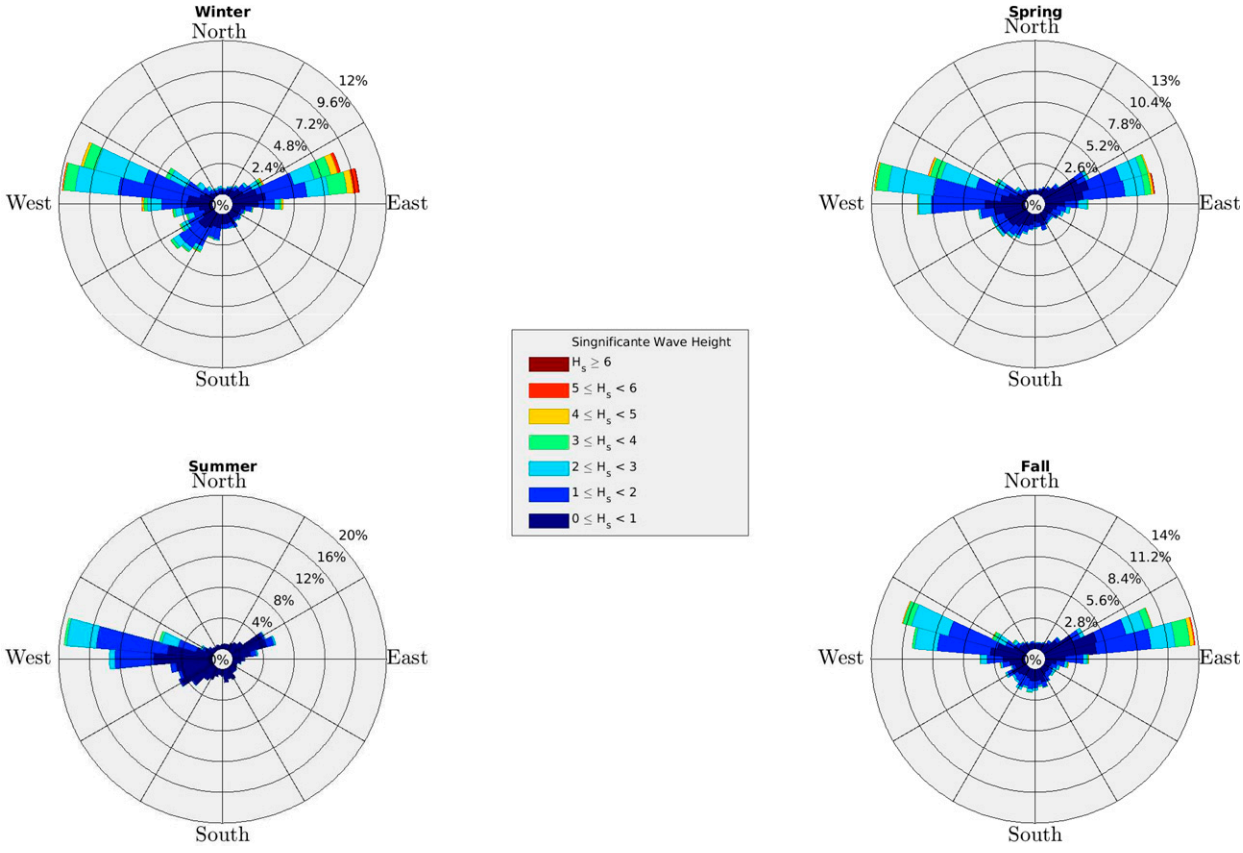

FIG. A1. Wave roses by season taken at P2. The roses were calculated using the wave parameters from WWIII.

degree, by horizontal changes in the water surface elevation (the baroclinic and barotropic contributions from the pressure gradient). Nonetheless, in shallow water regions (20–100 m) the ageostrophic component affects the entire water column, playing a major role in the geostrophic balance adjustment (Ekman-geostrophic adjustment) (Liu and Weisberg 2005a; Jia and Li 2012); thus, larger SOM arrays are needed in the joint analysis, together with additional variables such as the divergence of the velocity field when separating the current components.

It was possible to observe that the Stokes drift ($\mathbf{u}_s$) plays a relevant role on the near-surface ageostrophic current

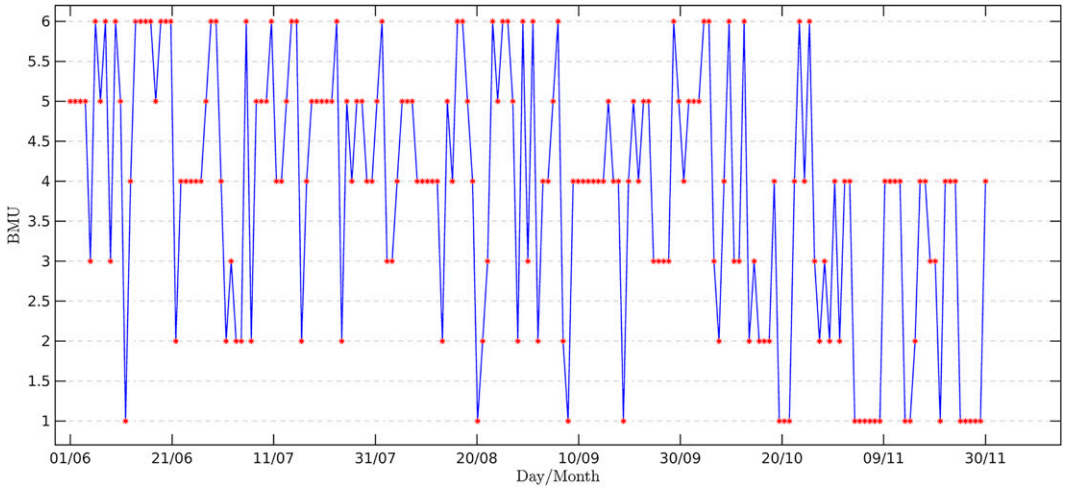

FIG. A2. The BMU time series for 3 × 2.

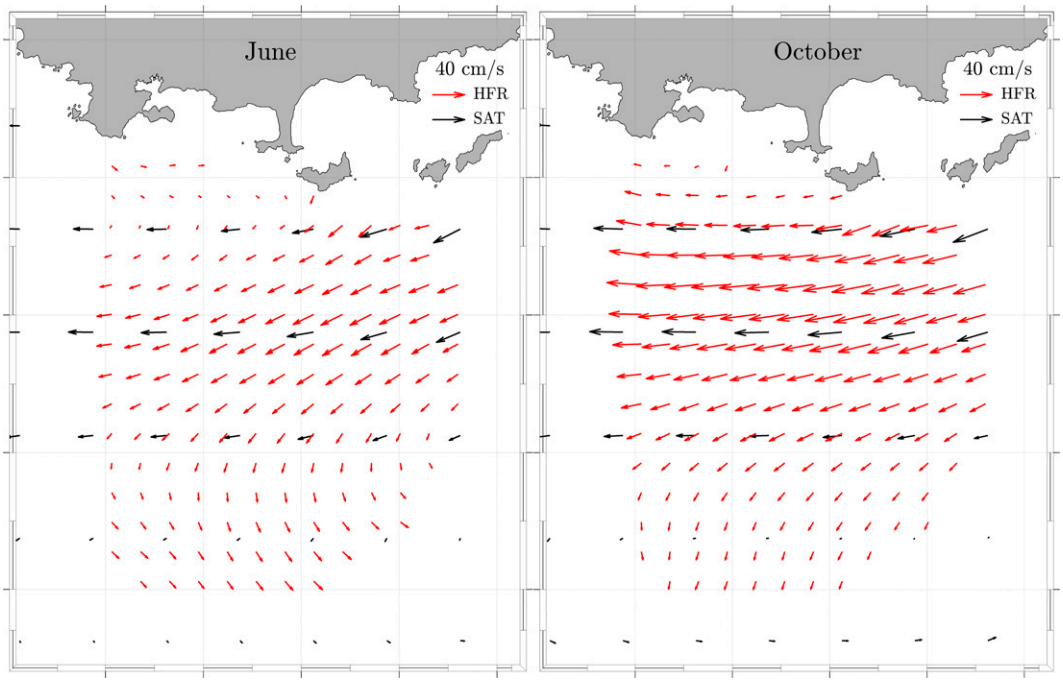

FIG. A3. Estimation of $\mathbf{u}_g$ using the whole dataset without applying the conditional averaging shown in section 5.

component ($\mathbf{u}_a$). Estimations indicate that u_s can be around 10% of u_a under weak wind conditions, and above 13% under moderate/strong wind conditions. This result contributes to the understanding of the role of $\mathbf{u}_s$ on $\mathbf{u}_a$, since to our knowledge, very few quantitative analysis based on in situ data have been performed [e.g., Tamtare et al. (2022) or Ardhuin et al. (2009)]. The wave contribution has been, previously, assumed negligible or too small (Berta et al. 2018; Morales-Márquez et al. 2021) to be evaluated individually in the ageostrophic component (Chang et al. 2012; van der Mheen et al. 2020).

SOM can be seen as a robust technique to extract dominant patterns from oceanographic information, including nonlinear processes. In addition, its low computational cost along with the capability to capture correlated physics-based processes (like wind and currents) makes it an efficient tool to analyze large amounts of data at sea, compared to time-demanding computational methods, such as ocean numerical modeling or supervised neural networks.

Finally, the novelty in this work is the specific use of a neuronal network method, more and more widespread in oceanography (Sinha and Abernathey 2021), to identify and assess the different components of the surface current. Our results open a new avenue for the validation of satellite data and their extension near the coast, but also suggest new insight for the wind and wave-induced components crucial for Lagrangian transport applications.

Acknowledgments. A. Cáceres-Euse and the upgrade of the WERA HFR system in Toulon has been funded by the research projects SICOMAR-PLUS and SINAPSI, Interreg Italia-Francia Marittimo 2014/2020. N. Bourg was funded by SHAREMED Interreg project. The HFR is part of the Mediterranean Ocean Observation Service for the Environment (MOOSE) French network. We thank the Parc National de Port-Cros (PNPC) for its support and hosting of our radar transmitter in Porquerolles Island. We also thank the "Association Syndicale des Propriétaires du Cap Bénat" (ASPCB) for allowing our receiver array at the Cap Bénat as well as the Group Military Conservation and the Marine Nationale for hosting our radar installation in

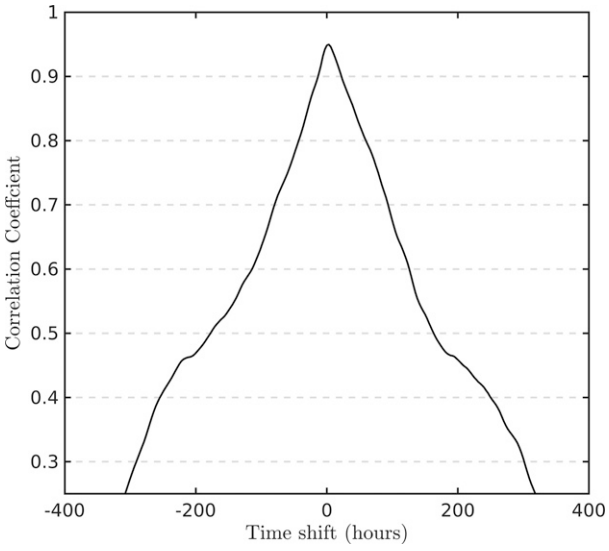

FIG. A4. Surface current-wind cross correlation once $\mathbf{u}_g$ was removed from $\mathbf{u}_t$.

Fort Peyras. We would like to thank the comments from the handling editor and the three anonymous reviewers that helped to improve this manuscript.

Data availability statement. The data presented herein are available upon request to the author at anne.molcard@univ-tln.fr and the quasi-real-time HFR maps through the web page hfradar.univ-tln.fr/.

APPENDIX

Supplementary Figures

This appendix presents Figs. A1–A4.

REFERENCES

Albuquerque, J., J. Antolínezm, A. Rueda, F. J. Méndez, and G. Coco, 2018: Directional correction of modeled sea and swell wave heights using satellite altimeter data. *Ocean Modell.*, **131**, 103–114, https://doi.org/10.1016/j.ocemod.2018.09.001.

Alvera-Azcárate, A., A. Barth, M. Rixen, and J. Beckers, 2005: Reconstruction of incomplete oceanographic data sets using empirical orthogonal functions: Application to the Adriatic sea surface temperature. *Ocean Modell.*, **9**, 325–346, https://doi.org/10.1016/j.ocemod.2004.08.001.

Ardhuin, F., L. Marié, N. Rascle, P. Forget, and A. Roland, 2009: Observation and estimation of Lagrangian, Stokes, and Eulerian currents induced by wind and waves at the sea surface. *J. Phys. Oceanogr.*, **39**, 2820–2838, https://doi.org/10.1175/2009JPO4169.1.

Berta, M., and Coauthors, 2018: Wind-induced variability in the Northern Current (northwestern Mediterranean sea) as depicted by a multi-platform observing system. *Ocean Sci.*, **14**, 689–710, https://doi.org/10.5194/os-14-689-2018.

Bourg, N., and A. Molcard, 2021: Northern boundary current variability and mesoscale dynamics: A long-term HFR monitoring in the north-western Mediterranean Sea. *Ocean Dyn.*, **71**, 851–870, https://doi.org/10.1007/s10236-021-01466-9.

Brousseau, P., Y. Seity, D. Ricard, and J. Léeger, 2016: Improvement of the forecast of convective activity from the AROME-France system. *Quart. J. Roy. Meteor. Soc.*, **142**, 2231–2243, https://doi.org/10.1002/qj.2822.

Bye, J. A., 1967: The wave-drift current. *J. Mar. Res.*, **25**, 95–102.

Carret, A., F. Birol, C. Estournel, B. Zakardjian, and T. Testor, 2019: Synergy between in situ and altimetry data to observe and study Northern Current variations (NW Mediterranean Sea). *Ocean Sci.*, **15**, 269–290, https://doi.org/10.5194/os-2018-76.

Chang, Y. C., G. Y. Chen, R. S. Tseng, L. R. Centurioni, and P. C. Chu, 2012: Observed near-surface currents under high wind speeds. *J. Geophys. Res.*, **117**, C11026, https://doi.org/10.1029/2012JC007996.

Chavanne, C., 2018: Do high-frequency radars measure the wave-induced Stokes drift? *J. Atmos. Oceanic Technol.*, **35**, 1023–1031, https://doi.org/10.1175/JTECH-D-17-0099.1.

Clarke, A., and S. Van Gorder, 2018: The relationship of near-surface flow, Stokes drift and the wind stress. *J. Geophys. Res. Oceans*, **123**, 4680–4692, https://doi.org/10.1029/2018JC014102.

Donlon, C., 2013: ESA Data User Element (DUE) GlobCurrent user requirement document (URD). ESA Tech. Rep. EOP-SM/2451/CD-cd, 137 pp.

Dritschel, D. G., N. Paldor, and A. Constantin, 2020: The Ekman spiral for piecewise-uniform viscosity. *Ocean Sci.*, **16**, 1089–1093, https://doi.org/10.5194/os-16-1089-2020.

Dumas, D., and C.-A. Guérin, 2020: Self-calibration and antenna grouping for bistatic oceanographic high-frequency radars. arXiv, 2005.10528, https://arxiv.org/abs/2005.10528.

——, A. Gramoullé, C.-A. Guérin, A. Molcard, Y. Ourmières, and B. Zakardjian, 2020: Multistatic estimation of high-frequency radar surface currents in the region of Toulon. *Ocean Dyn.*, **70**, 1485–1503, https://doi.org/10.1007/s10236-020-01406-z.

Fernandez, D. M., J. F. Vesecky, and C. Teague, 1996: Measurements of upper ocean surface current shear with high-frequency radar. *J. Geophys. Res.*, **101**, 28 615–28 625, https://doi.org/10.1029/96JC03108.

Garrat, J. R., 1997: *The Atmospheric Boundary Layer*. Cambridge University Press, 316 pp.

Guérin, C.-A., D. Dumas, A. Gramoullé, C. Quentin, M. Saillard, and A. Molcard, 2019: The multistatic oceanographic HF radar network in Toulon. *IEEE 2019 Int. Radar Conf.*, Toulon, France, IEEE, https://doi.org/10.1109/RADAR41533.2019.

Guihou, K., J. Marmain, Y. Ourmières, A. Molcard, B. Zakardjian, and P. Forget, 2013: A case study of the mesoscale dynamics in the north-western Mediterranean Sea: A combined data–model approach. *Ocean Dyn.*, **63**, 793–808, https://doi.org/10.1007/s10236-013-0619-z.

Hernández-Carrasco, I., and A. Orfila, 2018: The role of an intense front on the connectivity of the western Mediterranean Sea: The Cartagena-Tenes front. *J. Geophys. Res. Oceans*, **123**, 4398–4422, https://doi.org/10.1029/2017JC013613.

——, L. Solabarrieta, A. Rubio, G. Esnaola, E. Reyes, and A. Orfila, 2018: Impact of HF radar current gap-filling methodologies on the Lagrangian assessment of coastal dynamics. *Ocean Sci.*, **14**, 827–847, https://doi.org/10.5194/os-14-827-2018.

Jia, P., and M. Li, 2012: Dynamics of wind-driven circulation in a shallow lagoon with strong horizontal density gradient. *J. Geophys. Res.*, **117**, C05013, https://doi.org/10.1029/2011JC007475.

Kenyon, K., 1969: Stokes drift for random gravity waves. *J. Geophys. Res.*, **74**, 6991–6994, https://doi.org/10.1029/JC074i028p06991.

Kirwan, A. D., G. McNally, S. Pazan, and R. Wert, 1979: Analysis of surface current response to wind. *J. Phys. Oceanogr.*, **9**, 401–412, https://doi.org/10.1175/1520-0485(1979)009<0401:AOSCRT>2.0.CO;2.

Kubota, M., 1994: A mechanism for the accumulation of floating marine debris north of Hawaii. *J. Phys. Oceanogr.*, **24**, 1059–1064, https://doi.org/10.1175/1520-0485(1994)024<1059:AMFTAO>2.0.CO;2.

Kumar, N., D. L. Cahl, S. C. Crosby, and G. Voulgaris, 2017: Bulk versus spectral wave parameters: Implications on Stokes drift estimates, regional wave modeling, and HF radars applications. *J. Phys. Oceanogr.*, **47**, 1413–1431, https://doi.org/10.1175/JPO-D-16-0203.1.

Kundu, P., I. Cohen, and D. Dowling, 2012: *Fluid Mechanics*. 5th ed. Academic Press, 891 pp.

Lira-Loarca, A., A. Cáceres-Euse, F. De-Leo, and G. Besio, 2022: Wave modeling with unstructured mesh for hindcast, forecast and wave hazard applications in the Mediterranean Sea. *Appl. Ocean Res.*, **122**, 103118, https://doi.org/10.1016/j.apor.2022.103118.

Liu, Y., and R. H. Weisberg, 2005a: Momentum balance diagnoses for the west Florida shelf. *Cont. Shelf Res.*, **25**, 2054–2074, https://doi.org/10.1016/j.csr.2005.03.004.

——, and ——, 2005b: Patterns of ocean current variability on the west Florida shelf using the self-organizing map. *J. Geophys. Res.*, **110**, C06003, https://doi.org/10.1029/2004JC002786.

——, and ——, 2007: Ocean currents and sea surface heights estimated across the west Florida shelf. *J. Phys. Oceanogr.*, **37**, 1697–1713, https://doi.org/10.1175/JPO3083.1.

——, ——, and C. N. K. Mooers, 2006: Performance evaluation of the self-organizing map for feature extraction. *J. Geophys. Res.*, **111**, C05018, https://doi.org/10.1029/2005JC003117.

——, ——, and L. K. Shay, 2007: Current patterns on the west Florida shelf from joint self-organizing map analyses of HF radar and ADCP data. *J. Atmos. Oceanic Technol.*, **24**, 702–712, https://doi.org/10.1175/JTECH1999.1.

Lorente, P., and Coauthors, 2022: Coastal high-frequency radars in the Mediterranean—Part 1: Status of operations and a framework for future development. *Ocean Sci.*, **18**, 761–795, https://doi.org/10.5194/os-18-761-2022.

Mao, Y., and M. L. Heron, 2008: The influence of fetch on the response of surface currents to wind studies by HF ocean surface radar. *J. Phys. Oceanogr.*, **38**, 1107–1121, https://doi.org/10.1175/2007JPO3709.1.

Martinez, E., K. Maamaatuaiahutapua, and V. Taillandier, 2009: Floating marine debris surface drift: Convergence and accumulation toward the South Pacific subtropical gyre. *Mar. Pollut. Bull.*, **58**, 1347–1355, https://doi.org/10.1016/j.marpolbul.2009.04.022.

Mazoyer, C., H. Vanneste, C. Dufresne, Y. Ourmières, M. G. Magaldi, and A. Molcard, 2020: Impact of wind-driven circulation on contaminant dispersion in a semi-enclosed bay. *Estuarine Coastal Shelf Sci.*, **233**, 106529, https://doi.org/10.1016/j.ecss.2019.106529.

Mihanović, H., S. Cosoli, I. Vilibić, D. Ivankovi, V. Dadić, and M. Gačić, 2011: Surface current patterns in the northern Adriatic extracted from high-frequency radar data using self-organizing map analysis. *J. Geophys. Res.*, **116**, C08033, https://doi.org/10.1029/2011JC007104.

Millot, C., 1989: La circulation générale en Méditerranée occidentale: Aperçu de nos connaissances et projets d'études. *Cont. Shelf Res.*, **98**, 497–515, https://doi.org/10.3406/geo.1989.20925.

——, 1999: Circulation in the western Mediterranean Sea. *J. Mar. Syst.*, **20**, 423–442, https://doi.org/10.1016/S0924-7963(98)00078-5.

Molcard, A., A. Gramoullé, C. Mazoyer, N. Bourg, and Y. Ourmières, 2021: Dynamics and transport from the boundary Northern Current toward the Toulon Bay: Multi-platform observations and downscaling modelling approaches. *Ocean Dyn.*, **71**, 993–1009, https://doi.org/10.1007/s10236-021-01479-4.

Morales-Márquez, V., I. Hernández-Carrasco, G. Simarro, V. Rossi, and A. Orfila, 2021: Regionalizing the impacts of wind and wave-induced currents on surface ocean dynamics: A long-term variability analysis in the Mediterranean Sea. *J. Geophys. Res. Oceans*, **126**, e2020JC017104, https://doi.org/10.1029/2020JC017104.

Novelli, G., M. Guigand, C. Cousin, E. H. Ryan, N. J. M. Laxague, H. Dai, B. K. Haus, and T. M. Özgökmen, 2017: A biodegradable surface drifter for ocean sampling on a massive scale. *J. Atmos. Oceanic Technol.*, **34**, 2509–2532, https://doi.org/10.1175/JTECH-D-17-0055.1.

Onink, V., D. Wichmann, P. Delandmeter, and E. van Sebille, 2019: The role of Ekman currents, geostrophy, and Stokes drift in the accumulation of floating microplastic. *J. Geophys. Res. Oceans*, **124**, 1474–1490, https://doi.org/10.1029/2018JC014547.

Orfila, A., C. P. Urbano-Latorre, J. M. Sayol, S. Gonzalez-Montes, A. Cáceres-Euse, I. Hernández-Carrasco, and A. G. Muñoz, 2021: On the impact of the Caribbean Counter Current in the Guajira upwelling system. *Front. Mar. Sci.*, **8**, 626823, https://doi.org/10.3389/fmars.2021.626823.

Ourmières, Y., B. Zakardjian, K. Béranger, and C. Langlais, 2011: Assessment of a NEMO-based downscaling experiment for the north-western Mediterranean region: Impacts on the Northern Current and comparison with ADCP data and altimetry products. *Ocean Modell.*, **39**, 386–404, https://doi.org/10.1016/j.ocemod.2011.06.002.

——, J. Mansui, A. Molcard, F. Galgani, and P. Isabelle, 2018: The boundary current role on the transport and stranding of floating marine litter: The French Riviera case. *Cont. Shelf Res.*, **155**, 11–20, https://doi.org/10.1016/j.csr.2018.01.010.

Pedlosky, J., 1987: *Geophysical Fluid Dynamics*. Springer-Verlag, 710 pp.

Petrenko, A. A., 2003: Variability of circulation features in the Gulf of Lion NW Mediterranean Sea. Importance of inertial currents. *Oceanol. Acta*, **26**, 323–338, https://doi.org/10.1016/S0399-1784(03)00038-0.

Polton, J. A., D. M. Lewis, and S. E. Belcher, 2005: The role of wave-induced Coriolis–Stokes forcing on the wind-driven mixed layer. *J. Phys. Oceanogr.*, **35**, 444–457, https://doi.org/10.1175/JPO2701.1.

Poulain, P.-M., M. Menna, and E. Mauri, 2012: Surface geostrophic circulation of the Mediterranean Sea derived from drifter and satellite altimeter data. *J. Phys. Oceanogr.*, **42**, 973–990, https://doi.org/10.1175/JPO-D-11-0159.1.

Rascle, N., and F. Ardhuin, 2009: Drift and mixing under the ocean surface revisited: Stratified conditions and model-data comparisons. *J. Geophys. Res.*, **114**, C02016, https://doi.org/10.1029/2007JC004466.

Rey, V., C. Dufresne, J.-L. Fuda, D. Mallarino, T. Missamou, C. Paugam, G. Rougier, and I. Taupier-Letage, 2020: On the use of long-term observation of water level and temperature along the shore for a better understanding of the dynamics: Example of Toulon area, France. *Ocean Dyn.*, **70**, 913–933, https://doi.org/10.1007/s10236-020-01363-7.

Reyes, E., and Coauthors, 2022: Coastal high-frequency radars in the Mediterranean—Part 2: Applications in support of science priorities and societal needs. *Ocean Sci.*, **18**, 797–837, https://doi.org/10.5194/os-18-797-2022.

Rio, M. H., S. Mulet, and N. Picot, 2014: Beyond GOCE for the ocean circulation estimate: Synergetic use of altimetry, gravimetry, and in situ data provides new insight into geostrophic and Ekman currents. *Geophys. Res. Lett.*, **41**, 8918–8925, https://doi.org/10.1002/2014GL061773.

Roach, C. J., H. E. Phillips, N. L. Bindoff, and S. R. Rintoul, 2015: Detecting and characterizing Ekman currents in the Southern Ocean. *J. Phys. Oceanogr.*, **45**, 1205–1223, https://doi.org/10.1175/JPO-D-14-0115.1.

Sauvage, C., C. L. Brossier, and M.-N. Bouin, 2021: Towards kilometer-scale ocean–atmosphere–wave coupled forecast: A case study on a Mediterranean heavy precipitation event. *Atmos. Chem. Phys.*, **21**, 11 857–11 887, https://doi.org/10.5194/acp-21-11857-2021.

Shay, L., J. Martinez-Pedraja, T. Cook, B. Haus, and R. Weisberg, 2007: High-frequency radar mapping of surface currents using WERA. *J. Atmos. Oceanic Technol.*, **24**, 484–503, https://doi.org/10.1175/JTECH1985.1.

Shrira, V. I., and P. Forget, 2015: On the nature of near-inertial oscillations in the uppermost part of the ocean and a possible route toward HF radar probing of stratification. *J. Phys. Oceanogr.*, **45**, 2660–2678, https://doi.org/10.1175/JPO-D-14-0247.1.

——, and R. B. Almelah, 2020: Upper-ocean Ekman current dynamics: A new perspective. *J. Fluid Mech.*, **887**, A24, https://doi.org/10.1017/jfm.2019.1059.

Sinha, A., and R. Abernathey, 2021: Estimating ocean surface currents with machine learning. *Front. Mar. Sci.*, **8**, 672477, https://doi.org/10.3389/fmars.2021.672477.

Stewart, R., and J. W. Joy, 1974: HF radio measurement of surface currents. *Deep-Sea Res.*, **21**, 1037–1049, https://doi.org/10.1016/0011-7471(74)90066-7.

Tamtare, T., D. Dumont, and C. Chavanne, 2022: The Stokes drift in ocean surface drift prediction. *J. Oper. Oceanogr.*, **15**, 156–168, https://doi.org/10.1080/1755876X.2021.1872229.

Tolamn, H., 2009: User manual and system documentation of WAVEWATCH III version 3.14. MMAB Rep. 276, 220 pp., http://polar.ncep.noaa.gov/mmab/papers/tn276/MMAB_276.pdf.

van der Mheen, M., C. Pattiaratchi, S. Cosoli, and M. Wandres, 2020: Depth-dependent correction for wind-driven drift current in particle tracking applications. *Front. Mar. Sci.*, **7**, 305, https://doi.org/10.3389/fmars.2020.00305.

Vesanto, J., J. Himberg, E. Alhoniemi, and J. Parhankangas, 2000: SOM Toolbox for MATLAB 5. SOM Toolbox Team Rep. A57, 60 pp.

Vilibić, I., and Coauthors, 2016: Self-organizing maps-based ocean currents forecasting system. *Sci. Rep.*, **6**, 22924, https://doi.org/10.1038/srep22924.